Characterization of the Myosin-Based Source for Second-Harmonic Generation from Muscle Sarcomeres

Sergey V. Plotnikov,*‡ Andrew C. Millard,†‡ Paul J. Campagnola,†‡ and William A. Mohler*‡
*Department of Genetics and Developmental Biology, †Department of Cell Biology, and ‡Center for Cell Analysis and Modeling, University of Connecticut Health Center, Farmington, Connecticut 06030-3301

ABSTRACT   Several biologically important protein structures give rise to strong second-harmonic generation (SHG) in their native context. In addition to high-contrast optical sections of cells and tissues, SHG imaging can provide detailed structural information based on the physical constraints of the optical effect. In this study we characterize, by biochemical and optical analysis, the critical structures underlying SHG from the complex muscle sarcomere. SHG emission arises from domains of the sarcomere containing thick filaments, even within nascent sarcomeres of differentiating myocytes. SHG from isolated myofibrils is abolished by extraction of myosin, but is unaffected by removal or addition of actin filaments. Furthermore, the polarization dependence of sarcomeric SHG is not affected by either the proportion of myosin head domains or the orientation of myosin heads. By fitting SHG polarization anisotropy readings to theoretical response curves, we find an orientation for the elemental harmonophore that corresponds well to the pitch of the myosin rod α-helix along the thick filament axis. Taken together, these data indicate that myosin rod domains are the key structures giving SHG from striated muscle. This study should guide the interpretation of SHG contrast in images of cardiac and skeletal muscle tissue for a variety of biomedical applications.

INTRODUCTION

Second harmonic generation (SHG) imaging, a recently introduced nonlinear optical microscopy technique, is based on interaction of a strong laser beam with highly polarizable matter in a noncentrosymmetric molecular organization. Such interaction results in emission of photons with exactly twice the energy of the incident laser (see reviews (1,2)). Many animal tissue structures can be imaged via SHG microscopy, by virtue of intrinsic contrast generated by filamentous proteins: collagen fibrils in connective tissues, microtubules, and the actomyosin lattice of muscle cells (3–16). SHG microscopy benefits from intrinsic optical sectioning, deep penetration into three-dimensional samples, and the presence of endogenous sources in live, untreated specimens. SHG can be imaged simultaneously with distinct two-photon-excited fluorescence (2PEF) signals from one or more endogenous or exogenous labels (17). These attributes underlie the potential of SHG imaging in biomedical applications including native pathology and high-resolution in vivo imaging or spectroscopy via fiber-based laser-scanning probes (18).

Knowing the source of the SHG will be a fundamental requirement for any such applications. Whereas the component proteins that give rise to SHG in collagen fibrils and microtubules are clearly collagen and tubulin, the muscle sarcomere has a more complex structure comprising three distinct forms of major filaments and dozens of proteins (19). Thick myosin filaments, thin actin filaments, titin filaments, or the combination of these, could comprise the SHG harmonophore (Fig. 1). Because these filaments undergo changes in conformation and the extent of their interaction

during the contraction and extension of muscle, it is possible that SHG might vary quantifiably during contraction, allowing the use of SHG spectroscopy to measure sarcomeric activity. In addition, polarization or intensity of the SHG signal may quantifiably indicate the composition of new or changing myofibrils.

Previous characterization of the birefringence of myofibrils has concluded that contrast within the anisotropic A band, which corresponds spatially to sarcomeric SHG, is influenced by the overlap of thick and thin filaments (20,21). The similarities between SHG and polarization microscopy images are suggestive of similar sources of contrast. Yet, the two modalities have already been shown to highlight nonidentical sets of structures in nematode muscle cells (5). Correlations between these two optical phenomena without direct experimentation is therefore not necessarily tenable.

Previous evidence from our group has indicated that genetic disruption of myosin heavy chain genes (MHC) in *Caenorhabditis elegans* reduces sarcomeric SHG and that the localization of SHG in *C. elegans* muscle corresponded to a region containing thick filaments (5). However, the striation pattern of these mutant animals developed completely abnormally, preventing us from concluding absolutely that MHC alone, and not other features of normal sarcomeric structure, was the critical harmonophore for SHG.

Because of the crucial importance of understanding the molecular source of sarcomeric SHG for any interpretation of experimental or medical imaging data, we have undertaken here an exhaustive characterization of SHG from isolated myofibrils. These preparations have allowed us to perform biochemical and pharmacological manipulations of the various sarcomeric filaments and myosin motor domains while imaging, and enabled high-resolution analysis of the
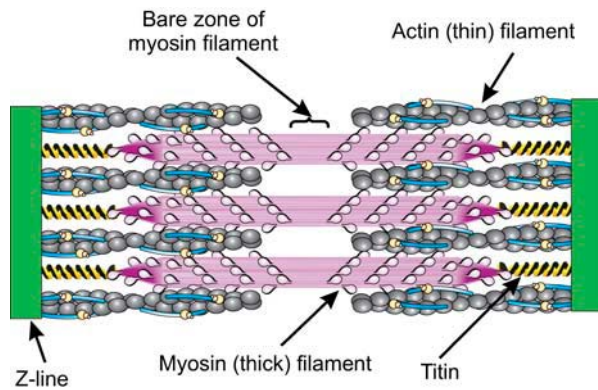
FIGURE 1 Schematic representation of sarcomere organization. The major protein filament components are indicated. Relative lengths of filaments are accurately proportioned in this cartoon.

polarization anisotropy of SHG within individual sarcomeres. This work leads to our conclusion that SHG arises from within the coiled rod region of myosin thick filaments and that SHG, although indicative of contraction and extension in images of muscle, does not depend upon the functional state of myosin head domains or the actin filaments with which they interact.

MATERIALS AND METHODS

Experimental microscope setup and imaging conditions

The nonlinear optical imaging systems used in our experiments were basically the same as described previously (5,22,23). Both systems were based on upright microscopes (Zeiss Axiovert or Olympus BX61) equipped with an Olympus FluoView 300 (Olympus, Melville, NY) scanning head and Coherent Mira 900 Ti-sapphire laser (Coherent, Santa Clara, CA). The average power at the sample plane varied from 10 to 50 mW. For image acquisition the following settings were usually used: image size 512×512 pixels, zoom $\times 2$, scan speed 10.2 μs/pixel, acquisition mode—Kalman average of three images. The excitation wavelength used was typically 900 nm, unless otherwise noted.

The SHG was collected in the forward direction, and a long working distance $40\times$, 0.8 N.A. water immersion objective lens and a 0.9 N.A. condenser were used for excitation and signal collection, respectively. The SHG signal is first reflected with a 450-nm hard reflector (TLM2; bandwidth ± 45 nm; CVI Laser, Albuquerque, NM), then isolated from the laser fundamental and any fluorescence by 1-mm color glass (BG-39) and a 450-nm bandpass filter (10 nm full width half-maximum), and detected by a photon-counting photomultiplier module (Hamamatsu 7421; Bridgewater, NJ).

For analysis of polarization dependence of SHG, the imaging system was slightly modified. The exciting laser beam was directed through a polarizing beamsplitter cube (PBS-930-050, CVI Laser) after leaving the scanning head. The translating specimen stage was replaced with a Zeiss or Olympus rotating stage, depending on the microscope base.

Isolation of myofibrils

Myofibrils from mouse leg and striated scallop adductor muscles were isolated according to Szent-Gyorgyi et al. (24) and Knight and Trinick (25) with slight modifications. All procedures were done at $+4°$C. The muscles

were dissected, cut into strips $\sim$0.5-cm wide, and washed several times with a specific washing solution (WS). For scallop muscles, WS contained 50 mM KCl, 2 mM MgCl$_2$, 10 mM imidazole-HCl, pH 7.0, 2 mM EGTA, 0.5 mM DTT, 0.1 mM PMSF. For mouse muscle, WS contained 150 mM NaCl, 2 mM MgCl$_2$, 10 mM imidazole-HCl, pH 7.0, 2 mM EGTA, 0.5 mM DTT, 0.1 mM PMSF. The muscles were soaked in 50% glycerol in WS for 20–24 h, exchanged to fresh glycerol solution, and stored at $-20°$C for up to 5 months. To isolate myofibrils the muscle samples were cut into smaller pieces and incubated 30 min in WS to remove excess glycerol. Samples were homogenized in WS for 30 s on ice with a Sorval Omni Mixer homogenizer (Omni International, Warrenton, VA). Myofibrils were collected by centrifugation at $4000 \times g$ for 10 min, and the pellet was washed three times in the same solution to remove cytoplasm components and incubated 20 min in WS containing 0.5% Triton X-100. The sample was again centrifuged at $4000 \times g$ for 10 min, and myofibrils were washed three more times as described above. The final myofibril suspension was filtered through 80-μm nylon gauze and the flow-through was diluted to a protein concentration 10 mg/ml. Bradford assay (Bio-Rad Laboratories, Hercules, CA) was used to determine protein concentration.

Line-scan imaging of contracting myofibrils

Myofibrils were adsorbed to the coverslip surface for these experiments to constrain them to the focal plane of SHG optical sectioning during contraction. An aliquot (0.5 ml) of isolated scallop myofibril suspension was placed into a glass bottom Petri dish (MatTek, Ashland, MA) and the dish was centrifuged at $4000 \times g$ for 10 min. Loosely attached myofibrils were removed by several washes of WS, and 2 ml of washing solution supplemented with 2 mM CaCl$_2$ was added to the dish. The microscope objective was immersed directly into the buffer for imaging. A single myofibril was selected using XY scanning mode and the central part of the myofibril was scanned longitudinally in time-lapse line-scan mode (zoom $\times 8$, scan region 200 pixels, scan speed 7 μs/pixel, and 1.4 lines/ms). To induce myofibril contraction, 1 ml of WS with 2 mM CaCl$_2$ and 15 mM MgATP was added to the dish during scanning. The acquired images were scaled in the time dimension to fit a printed page using ImageJ software (see below).

Culture of skeletal and cardiac myocytes

Primary cell cultures of chicken cardiac and skeletal myocytes were established from tissues of 7- and 10-day-old chicken embryos, respectively (26). The cells cultivated on coverslips were fixed with 4% paraformaldehyde in PBS, permeabilized for 10 min with 0.5% Triton X-100, and washed several times with PBS. Then the samples were used for immunostaining of α-actinin.

Visualization of α-actinin and actin

Samples of unfixed mouse myofibrils or cultivated cells prepared as described above were stained with mouse monoclonal anti-α-actinin antibody (Sigma-Aldrich, St. Louis, MO). To prevent nonspecific antibody binding the samples were treated for 1 h at 4°C with 2% BSA in PBS and then incubated for 1 h with primary antibody diluted in PBS (dilution 1:800). After several washes with WS, secondary antibody (AlexaFluor488 conjugated goat-anti-mouse, Molecular Probes, Eugene, OR) was added to the samples for 1 h, the unbound antibody was washed out, and the sample was imaged as described above.

To visualize filamentous actin, AlexaFluor488-phalloidin (1 mg/ml in methanol, Molecular Probes) was added to an aliquot of myofibrils at a dilution factor of 1:100, and the sample was incubated for 30 min at 4°C. Unbound phalloidin was removed by several cycles of centrifugation-resuspension in WS. Stained myofibrils were pipetted onto a polylysine-coated glass-bottomed Petri dish, and the dish was centrifuged at $3000 \times g$ for 5 min to attach myofibrils to the bottom. Fresh room-temperature WS was added to the dish and myofibrils were imaged immediately.

Extraction of F-actin with Ca^{2+}-insensitive gelsolin

Gelsolin was purified from bovine plasma according to Kurokawa et al. (27). The purified gelsolin was cleaved with thermolysin, as described by Hidalgo et al. (28). In our experiments the gelsolin fragments were not fractionated after cleavage.

Ca^{2+}-insensitive gelsolin was added to a suspension of scallop myofibrils and the samples were incubated at room temperature for time increments from 5 to 60 min. For samples analyzed by SDS-PAGE, 20 vol of WS were added to the sample to stop gelsolin action, and samples were centrifuged for 30 min at 20,000 × g. The supernatant was removed, and the pellet was washed two more times with 2 ml of WS. Finally, the pellet was dissolved in 25 μl of SDS-PAGE loading buffer, boiled for 2 min, and loaded onto a 12.5% SDS-PAGE gel using the discontinuous buffer system of Laemmli (29).

The gels were stained with Coomassie G-250 (Sigma), scanned using an Epson Perfection 636U scanner, and quantitative analysis was carried out with RFLPscan Plus Version 3.12 (Scananalytics, Fairfax, VA). Relative amounts of MHC, paramyosin, and actin were calculated from the protein peak area, neglecting small differences in the known dye-binding characteristics of various muscle proteins.

Incorporation of exogenous F-actin into scallop myofibrils

Exogenous actin was incorporated into myofibrils according to Sanger (30). G-actin conjugated with AlexaFluor488 (Molecular Probes) was diluted with G-buffer (5 mM Tris-HCl, pH 8.1, 0.2 mM CaCl2, 0.2 mM DTT, 0.2 mM ATP) to final concentration 0.5 mg/ml, and 30 μl of sample was added to a 30-μl aliquot of scallop myofibrils. After 20 min incubation at room temperature the myofibrils were collected by gentle centrifugation (5 min at 3000 × g), and unpolymerized actin was washed out by several cycles of centrifugation and resuspension in WS, as described above. The myofibrils were resuspended in 20 μl of WS, pipetted onto a microscope slide, and used for SHG/2PEF imaging.

Extraction of myosin filaments

Myosin filaments were extracted according to Zhukarev et al. (31). The myofibrils were attached to a polylysine-coated coverslip, as described above, and myosin was extracted with high ionic strength solution (0.6 M KCl, 10 mM Na pyrophosphate, 1 mM MgCl2, 10 mM imidazole-HCl pH 6.4).

Image analysis and quantitation for microscopy

For quantitative analysis of Olympus FluoView TIFF image files, we used ImageJ software (http://rsb.info.nih.gov/ij) extended with UCSD plugin collection (http://rsb.info.nih.gov/ij/plugins/ucsd.html). Measurement of the spatial distribution of SHG and fluorescence within sarcomeres was done on the central optical section of a myofibril, rotated horizontal and measured with the PlotProfile tool.

For measurement of polarization anisotropy, average-intensity z-projections of confocal stacks at each angle of rotation were generated. Projected images were rotated to achieve the same orientation of myofibrils in the image window, and the same region of interest (ROI) was selected within each image. The ROI was selected to include as little background as possible, and the ROI mean gray value was measured by the ImageJ "Measure tool".

RESULTS

SHG arises from the thick-filament zone of the sarcomere

Previous results using GFP-labeled myosin in *C. elegans* body wall muscle indicated that SHG is emitted from the region surrounding the sarcomeric M-line (5). To confirm the colocalization of SHG sources with myosin filaments in non-nematode striated muscle, we combined SHG with 2PEF microscopy. Simultaneous visualization of SHG with either α-actinin or actin (Fig. 2, *A* and *B*, respectively) allowed us to precisely determine the localization of SHG within the sarcomere. As in *C. elegans*, each sarcomere imaged at high magnification contained an SHG-bright double-band. The distance between anti-α-actinin-labeled stripes and the SHG-emitting bands varied, but we never observed colocalization of SHG and α-actinin (see Fig. 5), indicating that the broad dark band between SHG-bright zones contains the Z-line and thin filaments, as well as confirming that the dim stripe within an SHG-bright double-band contains the M-line.

Visualization of phalloidin-stained actin showed localized fluorescence in both the broad dark region containing Z-lines and the central dim zone (M-line) within SHG-bright double-bands. Phalloidin labeling has been previously shown
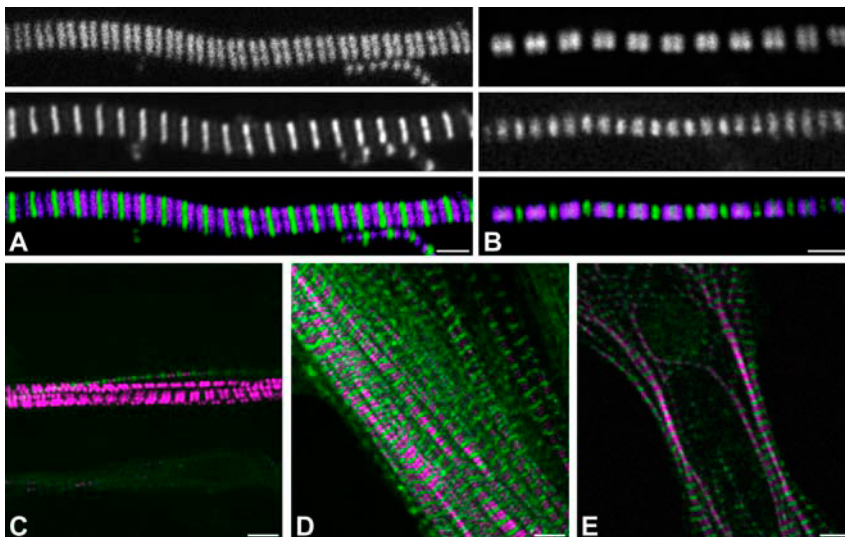

FIGURE 2 Localization of SHG to the thick-thin filament overlap zone of mature and developing sarcomeres. (*A*, *B*) Simultaneous visualization of SHG with either fluorescent immunostaining of α-actinin (*A*) or fluorescent phalloidin staining of actin (*B*) in isolated mouse myofibrils. SHG and fluorescence are shown on the top and middle panels, respectively. The bottom panels demonstrate the overlap of both channels (SHG is *purple*, fluorescence is *green*). (*C*, *D*) SHG (*purple*) and α-actinin (*green*) in chicken embryonic myoblasts cultured in vitro for 5 and 7 days, respectively. (*E*) SHG (*purple*) and α-actinin (*green*) in a chicken embryonic cardiomyocyte. Scale bars = 2.5 μm in panels *A* and *B*; 5 μm in panels *C*–*E*.

to occur only at the proximal and distal ends of sarcomeric thin filaments (32). Consistent with these reports, we found phalloidin localized in both the broad dark band and the central dim zone of SHG-imaged sarcomeres (Fig. 2 *B*). We concluded from the localization of SHG relative to both α-actinin and phalloidin staining, that SHG is produced by the central part of the sarcomere, where myosin filaments are localized (Fig. 1).

The SHG pattern found in nascent myofibrils within differentiating skeletal and cardiac myocytes was similar to that seen in myofibrils in mature muscle tissue (Fig. 2 *C–E*). Interestingly, we found that the development of harmonophores and the accumulation of α-actinin were not synchronous. Some nascent myofibrils produced SHG before α-actinin appeared at the Z-line, whereas in others α-actinin was organized periodically while no SHG was detectable.

SHG requires myosin but not actin

To determine whether thick filaments contribute to SHG either alone or in combination with actin, we correlated the lengths of sarcomeres (having different degrees of concomitant overlap of actin and myosin filaments) with two distinct measurements of the SHG pattern: a), the peak-to-peak distance between the centers of SHG bands within a sarcomere, and b), the width of each SHG-bright double-peak at its half-maximal intensity (see Fig. 3, *A* and *B*). The peak-to-peak distance *a*, corresponding to the center of the SHG double-band surrounding the M-line, changed little depending upon

sarcomere length. In contrast, the edge-to-edge width *b* of the full double-peak did vary linearly, but only in hypercontracted sarcomeres. Thus, neither the width nor the spacing of peaks in the SHG-emitting zone is dependent upon the extent of actin-myosin overlap in a sarcomere of intermediate or extended length, but the width does vary with the length of severely shortened sarcomeres. It is known that thick filaments retain a constant length in intermediate or extended sarcomeres, but undergo forced shortening in hypercontraction, due to pressure from the Z-lines (Fig. 3 *C* and Gordon et al. (33)). We therefore concluded that the shape of the SHG bands varies only with the length of the myosin filaments themselves, the hypercontracted case, without a significant influence from the overlap or myosin and actin filaments in normal and extended sarcomeres.

We next tested the direct contribution of thick and thin filaments to SHG by selective extraction of each component protein. Treatment of myofibrils with low-ionic strength pyrophosphate solution is known to cause specific disruption of myosin filaments, but does not destroy actin or titin filaments (34,35). We found that such extraction dramatically decreased SHG contrast from isolated myofibrils (Fig. 4), but did not change the periodicity of phalloidin-stained F-actin within myofibrils, indicating that actin filaments remain intact. To test the importance of actin directly, we performed a time course of selective extraction of thin filaments by applying Ca^{2+}-insensitive gelsolin; protein content of extracted myofibrils is demonstrated by SDS-PAGE analysis in Fig. 5 *A*. Imaging of myofibrils in parallel samples showed
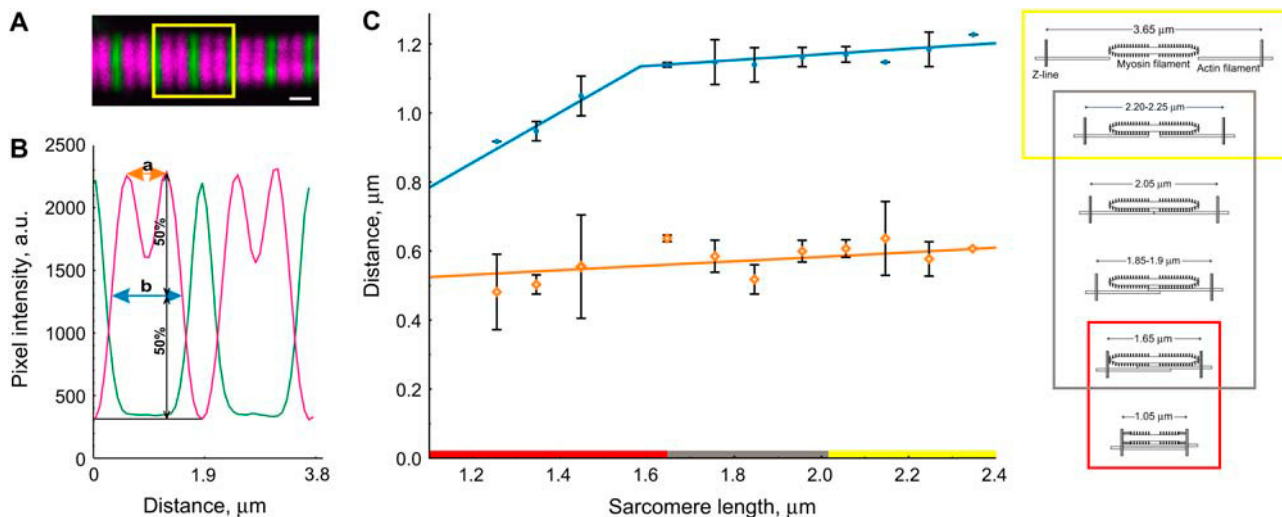

FIGURE 3 Dependence of SHG pattern on the extent of sarcomere contraction. (*A*) Example of an α-actinin-stained myofibril used for analysis (*purple*, SHG; *green*, α-actinin). The region profiled in panel *B* is enclosed in a yellow box. Scale bar = 1 μm. (*B*) Intensity profiles of SHG (*purple*) and fluorescence (*green*) from the selected pair of sarcomeres. Measured distances plotted in panel *C* are indicated. Distance *a* shows the peak-to-peak distance between SHG bands within a sarcomere; distance *b* shows the width of the SHG double-band at half-maximal intensity. (*C*) Correlation between sarcomere length (separation of α-actinin-stained Z-lines) with geometrical parameters *a* (*orange trace* and *points*) and *b* (*blue trace* and *points*) of the SHG pattern. The cartoon at right demonstrates known changes in overlap between actin and myosin filaments during progressive contraction. Colored boxes in the cartoon correspond to ranges of sarcomere length indicated on the *x* axis of the data graph (based on data from Gordon et al. (33)). For different sarcomere lengths shown, numbers of sarcomeres measured vary from 10 to 100 per data point. Error bars show mean ± SD.
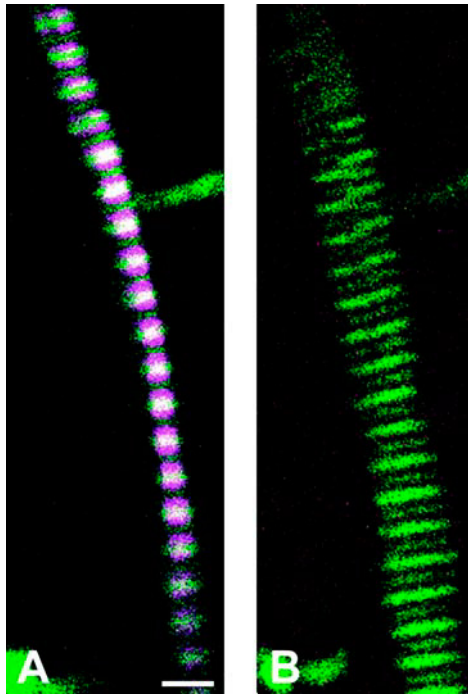
FIGURE 4 Dependence of SHG on myosin filaments. (*A*) SHG (*purple*) and fluorescence (*green*) from an isolated, unfixed mouse myofibril stained with AlexaFluor 488-phalloidin. (*B*) The same myofibril after myosin extraction. The SHG channel in panel *B* was collected with a fourfold increase in detector gain relative to panel *A*, but shows no sarcomeric signal. Scale bar = 5 μm.

that actin extraction did not change the intensity of SHG (Fig. 5 *B*). Similarly, incorporation of newly synthesized actin filaments into myofibrils produced no noticeable changes in SHG pattern or intensity (Fig. 5 *C*). These results confirmed that actin filaments do not influence the intensity or pattern of SHG from the sarcomere. Combining these various biochemical results, we concluded that the vast majority of SHG contrast in sarcomeres is generated by thick filament proteins.

SHG does not vary with the concentration or orientation of myosin heads

Because thick filaments contain both static rod domains and dynamic motor heads, we next tested the contribution of myosin head domains to SHG. To do so, we acquired profiles of SHG polarization anisotropy by rotating muscle specimens relative to the polarized laser beam of the microscope (Fig. 6 *A*) and recorded the changes in resulting SHG image intensity depending on the incident polarization (Fig. 6 *B*). This method yields a profile that is sensitive to the orientation of SHG-emitting dipoles in the myofibrils. We compared measurements from scallop myofibrils and *C. elegans* body wall muscle to determine the importance of myosin

head domains. A 15-fold difference in paramyosin (Pm) content is a major distinction between the protein compositions of thick filaments in these species; the Pm/MHC ratio is 0.067 for scallop and 1.0 for *C. elegans* striated muscle (36,37). Paramyosin contains coil domains but no motor head domains. Thus, a scallop thick filament contains an order of magnitude higher ratio of head/coil content than does a nematode thick filament. SHG increases as the square of the harmonophore density. Therefore, if myosin heads, which lie angled to the rod axis, contribute along with the rod to SHG, the polarization anisotropy of the two specimens should differ noticeably. However, we observed no significant difference in their SHG polarization anisotropy profiles (Fig. 6 *C*). Thus, changing the ratio of head/coil content does not affect the distribution of SHG-producing dipoles in thick filaments.

The contribution of the myosin heads to SHG was further tested by analysis of changes in SHG intensity and polarization anisotropy caused by disorganization of head domains in rigor-state myofibrils. Because strong SHG is produced only by ordered structures, significant decreases of SHG intensity should be caused by even slight randomization of the harmonophore order. The induction of contraction is an obvious way to disrupt ordered heads in rigor myofibril. Because there is no significant long-distance cooperativity between the movement of myosin heads during the contractile cycle (38), any SHG emitted from head domains should be abolished or reduced during muscle contraction. Using a rapid line-scan acquisition mode we found that SHG intensity does not change significantly during induced myofibril contraction (Fig. 7, *A* and *B*). We also used a non-hydrolyzable analog of ATP (AMP-PNP) to disrupt the orientation of head domains in rigor-state myofibrils (39). Although not all heads are typically dissociated by this treatment, the extreme sensitivity of SHG to harmonophore order should make even small effects on the SHG sources readily detectable. Isolated scallop myofibrils were treated with AMP-PNP and the SHG intensity was measured through a range of laser polarization angles. We found that the reduction of collective order among myosin heads resulted in no significant change in the polarization profile of SHG (Fig. 7 *C*). We concluded from this collection of experiments that myosin heads do not contribute detectably to emission of SHG from sarcomeres.

Sarcomeric SHG polarization anisotropy suggests sources lie within a coiled coil domain

Theory predicts that a given molecular arrangement of SHG-emitting dipoles will yield a characteristic profile of response to varying laser polarization. For this reason, polarization anisotropy data can be fitted to predicted response curves to estimate the geometrical disposition of source harmonophores within the molecular assembly. Theoretical considerations of the structure of protein filaments allow us to
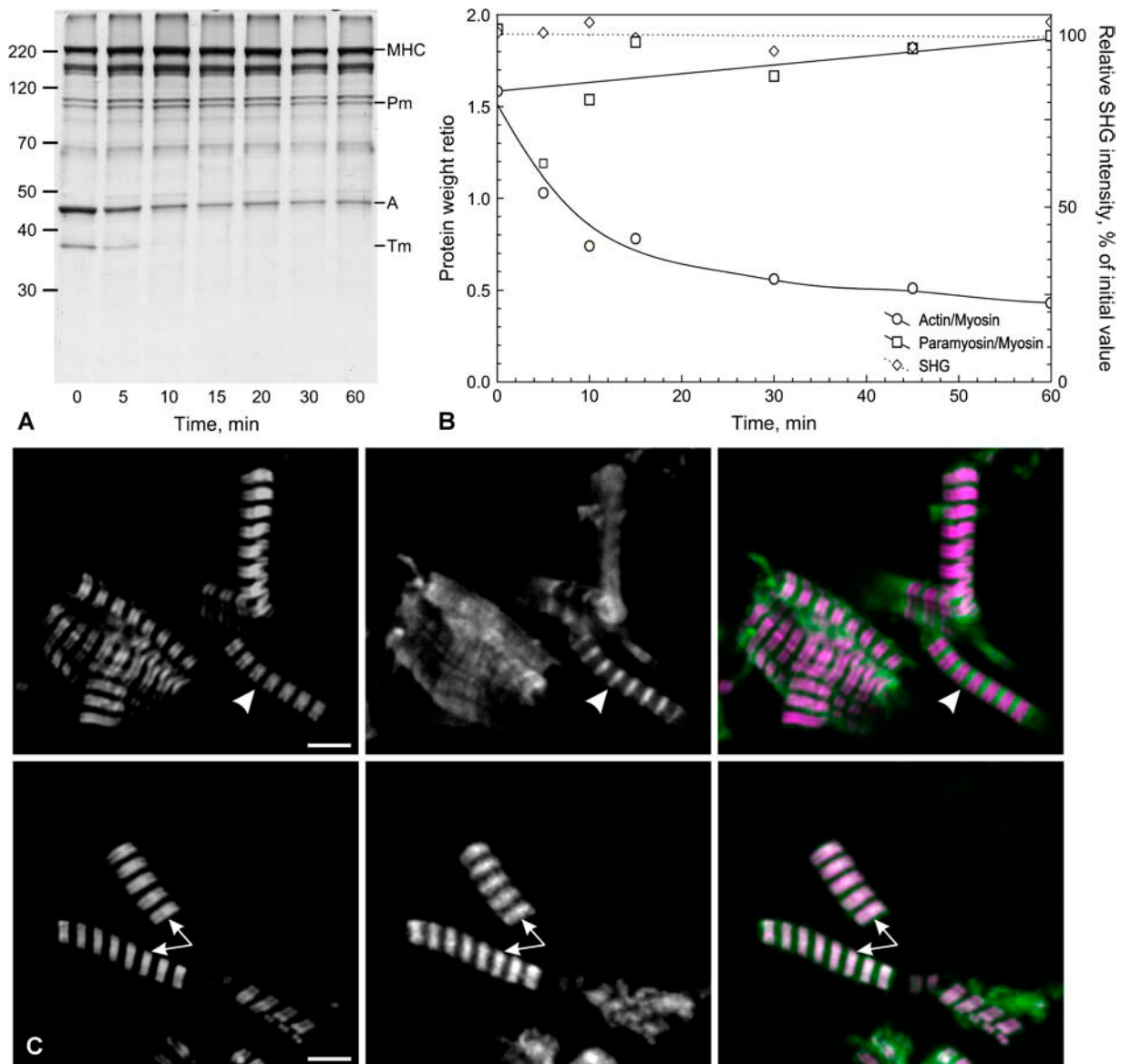
FIGURE 5 Independence of SHG on actin filaments. (*A*) Actin filament extraction from isolated scallop myofibrils by Ca^{2+}-insensitive gelsolin. Time-course analysis by SDS-PAGE shows content of actin (*A*), tropomyosin (*Tm*), paramyosin (*Pm*), and myosin heavy chain (*MHC*) in indicated bands. (*B*) Comparison of SHG image intensity by microscopy (*SHG*, *diamonds*, *dotted line*; right-hand *y* axis) with relative filament protein content analyzed by SDS-PAGE (actin/paramyosin, *circles*, *solid line*; paramyosin/myosin, *squares*, *solid line*; left-hand *y* axis). Imaging and gel analysis were done on parallel aliquots of myofibrils during treatment with gelsolin. (*C*) Unchanged SHG pattern after incorporation of newly synthesized actin filaments into isolated myofibrils. Top and bottom rows show two separate examples. SHG pattern (*left panels* and *purple* in color overlay) and the pattern of incorporated AlexaFluor488-actin (*center panels* and *green* in color overlay) are shown. Three different patterns of actin incorporation were observed: selective incorporation into A-disk (*arrows*), selective incorporation into I-disk (*arrowheads*), and relatively uniform distribution. None of these actin-incorporation patterns changed the SHG pattern from normal. Scale bar in panel *C* = 5 μm.

simplify the general case of SHG by assuming, based on our biochemical evidence, that SHG occurs within cylindrically symmetric arrangements of identical harmonophores (see Appendix: theoretical considerations).

In this case, the dependence of SHG upon laser polarization in the image plane reduces to only three independent variables, which we denote *a*, *b*, and *c*, by the convention of Stoller et al.

$$\mathbf{P}^{(2)} = a\,\mathbf{z}\,(\mathbf{z} \cdot \mathbf{E})^2 + b\mathbf{z}\,(\mathbf{E} \cdot \mathbf{E}) + c\,\mathbf{E}(\mathbf{z} \cdot \mathbf{E}),$$

where *a*, *b*, and *c* are numerical coefficients, $\mathbf{E}$ is the electric field, and $\mathbf{z}$ is the unit vector along the long axis of the cylinder (40,41,12). The values of these variables can be deduced by fitting the experimental SHG emission intensity as a function of laser polarization angle. This condition also allows us to calculate an angle, θ, which we interpret as the
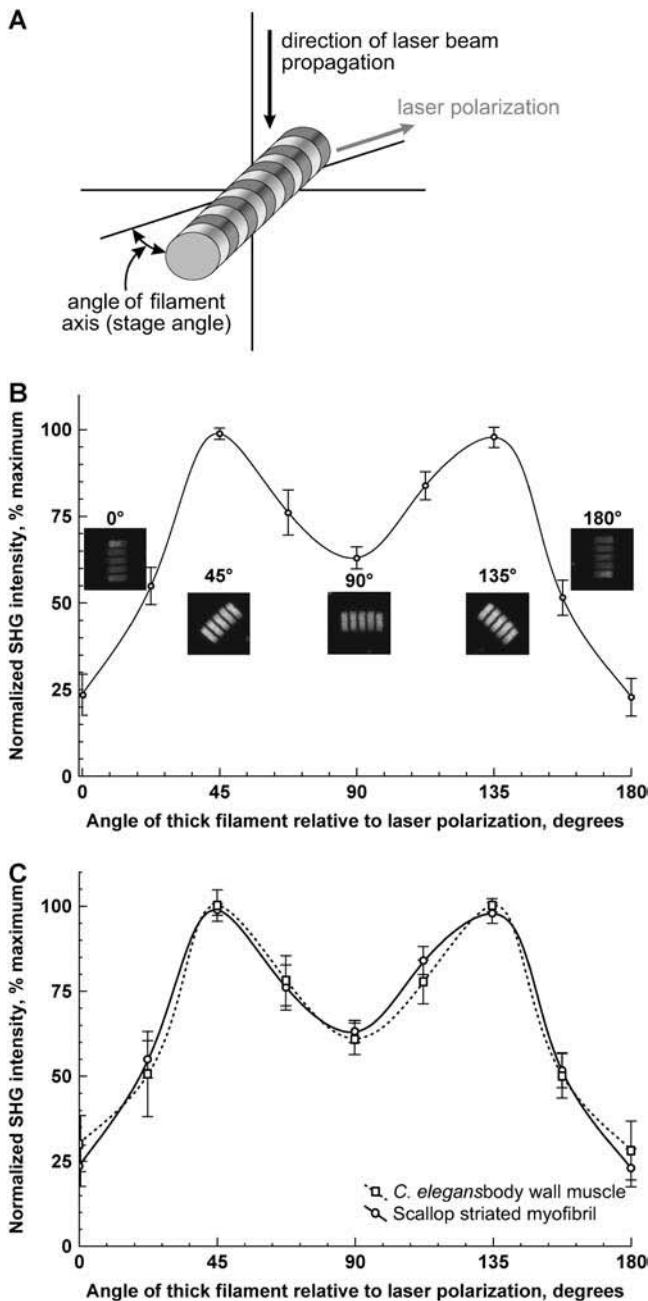
FIGURE 6 Polarization anisotropy of sarcomeric SHG. (*A*) Schematic showing the relative orientation of the specimen and the propagation and polarization axes of the excitation laser beam. (*B*) Profile of SHG intensity versus the relative angle of scallop myofibrils to laser polarization axis. Inserts show changes of SHG intensity with rotation relative to a fixed laser polarization. Error bars show mean ± SD. (*C*) Comparison of the polarization anisotropy of scallop striated myofibril and obliquely striated *C. elegans* body wall muscle. Error bars show mean ± SD.
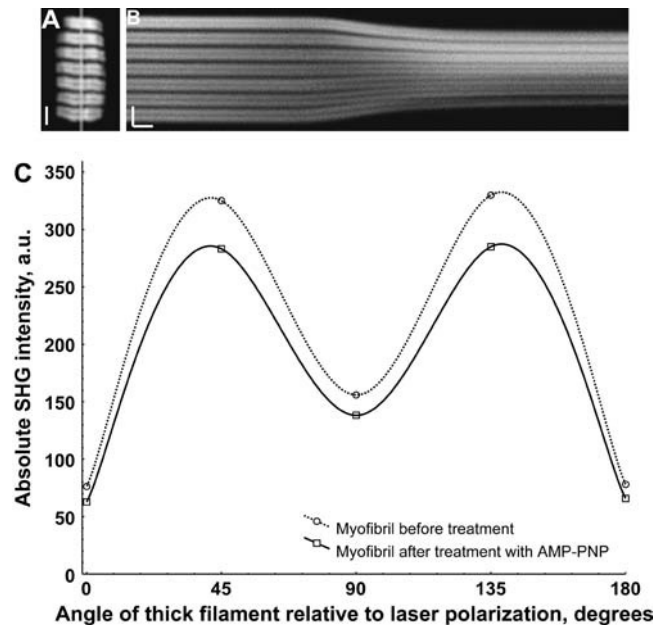

FIGURE 7 Independence of SHG on the state of myosin motor domains. (*A*) Example of single scallop myofibril selected for line-scan time-lapse imaging. The line marks the scanned region of the myofibril. Scale bar = 2.5 μm. (*B*) SHG line-scan imaging during contraction of the isolated scallop myofibril in panel *A*. Contraction speed of isolated myofibrils in our experiments varied between 0.2 and 0.45 μm/s/sarcomere. This value is almost 10 times slower than the published velocity of isotonic contraction in scallop myofibrils (57). However, we believe that this difference may be caused by adsorption of myofibrils on the glass surface, which should introduce increasing tension (nonisotonic) during contraction. Some changes of SHG intensity were observed at ends of myofibrils that moved out of the plane of section. Vertical (length) and horizontal (time) scale bars are 2.5 μm and 0.5 s, respectively. (*C*) Dissociation of myosin heads from actin filaments does not significantly affect the polarization anisotropy of isolated myofibrils. Anisotropy profiles are shown from a single myofibril both before and after addition of AMP-PNP. Relative susceptibility to varying laser polarization is unchanged, as absolute intensities at all angles are reduced by AMP-PNP treatment.

angle of maximum hyperpolarizability of the harmonophore relative to the long axis of the model cylinder (see Appendix: theoretical considerations). Our measurements of SHG from isolated myofibrils at 900-nm excitation gave $\theta = 61.2°$ (raw data shown in Fig. 6 *B*). This concurs with our geometrical analysis ($\theta = 67.2°$) of SHG polarization anisotropy extracted from 1230-nm-excited skeletal muscle by Chu et al. (12). Both of these values closely approximate the angle of the polypeptide chain in an α-helix relative to the helix axis, measured as 68.6° by x-ray diffraction (42). For comparison, our calculations of $\theta = 50.7°$ for tendon collagen fibrils imaged at 900 nm (our data), and $\theta = 49.5°$ for measurements by Stoller et al. (40) at 800 nm, coincide well with $\theta = 45.3°$, the known pitch of the polypeptide chain in the collagen glycine-proline helix (42). Two previous reports suggest that SHG sources lie within the amide bonds of polypeptide chains (43–45). Thus, we regard the calculated angle for myosin as a viable estimate of the arrangement of excitable dipoles within myofibrils. Because $\theta = 61.2°$ matches the pitch of the peptide coil of the myosin rod domain, and because SHG polarization response is insensitive to either the proportion or movement of motor head domains, we

concluded that sarcomeric SHG arises predominantly in the coiled rod portion of thick filaments.

DISCUSSION

Our results here, combined with data in previous publications, indicate that SHG from muscle tissue is emitted by myosin rods, and not by other filamentous components of myofibrils. When myosin is removed either by biochemical extraction or by genetic deletion, SHG is disrupted (5). In the current study, removal of myosin from myofibrils left sarcomere periodicity, and therefore much of the nonmyosin structure of sarcomeres, intact. Yet SHG was completely abolished. This result clearly indicates that neither actin (visible in fluorescence images of the extracted myofibrils) nor titin filaments (required to maintain the normal sarcomere spacing) can generate detectable SHG. Furthermore, neither extraction nor superdeposition of actin filaments in myofibrils had measurable effects on SHG. These experiments, combined with quantitative analysis of the dependence of SHG on thick filament length, clearly validate for the first time the hypothesis that myosin is the critical source of sarcomeric SHG.

Although myosin is the most dynamic component of the contractile apparatus, we find that SHG is quite stable, in both intensity and polarization dependence, even when myofibrils are subjected to changes in the enzymatic state, and therefore position, of the myosin motor head domains. This contrasts with a published hypothesis that correlates SHG with the distribution of heads along thick filaments (11). Furthermore, we find that SHG polarization anisotropy is unaffected by the coil/head ratio of invertebrate thick filaments. In addition, the calculated orientation of the source harmonophore, based on polarization analysis, coincides with the known pitches of distinct helices within the coil structures of both myosin and collagen. Taken together, these data suggest strongly that only the rod portion of the thick filament emits SHG.

Based on these conclusions, we can now note that all three strong second-harmonic emitting protein structures—collagen fibrils, myosin filaments, and microtubules—are currently modeled as rods in which the harmonophores form a shell around a central hollow or core of other molecules. (46–51,16). Thus, it is interesting to consider that the lack of imageable SHG from abundant solid or random-coil filaments (e.g., actin, titin, elastin) might be due either to lack of a shell-like geometry or to a subcritical diameter for the component filaments that make up the larger-order structure. This shell-form hypothesis could also explain the nonuniform SHG emission by the A-band of sarcomeres. It has been shown previously for both *C. elegans* body wall muscle (48) and scallop striated muscle (46) that the central M-line-proximal part of a myosin filament is solid and the tip is hollow. Lack of a shell geometry, in combination with centrosymmetry at the M-line, might explain the loss of SHG

at the center of each A-band. Although classical theory does not predict that SHG should depend on such hollow arrangements of harmonophores, Williams et al., have noted that the direction of SHG emission in collagen fibrils can be very dependent upon hollow-shell geometries (16). Furthermore, aspects of the existing theory of SHG must be expanded to accommodate the new collection of observations in complex protein arrays, as these structures have already been shown to exhibit optical responses in SHG that are quite different from those of inorganic crystals or interfaces (3,5).

Our new understanding of the sarcomeric SHG source better defines the possible applications of SHG in muscle physiology. The extent of contraction or extension of myofibrils can be measured in live cells without staining, with substantial advantages over classical polarization microscopy in imaging striations deep within muscle tissue samples. Thus, for example, fast shortening and lengthening movements of a single muscle cell should be measurable hundreds of microns deep within undissociated skeletal or cardiac tissue, by using rapid imaging or line scans along the cell's contractile axis (11,14). In our experiments we were able to image a single myofibril contraction with high spatial and temporal resolution. This resolution is sufficient for precise quantitative analysis of even fast muscle contractions. Our data also indicate that a constant level of contrast is maintained during all phases of the contraction cycle, simplifying the use of automated pattern analysis in processing such data. The absence of physiologically relevant effects on the intensity or polarization dependence of muscle SHG, however, seem to discount the possible use of SHG spectroscopy to measure muscle contraction.

Additionally, data in this article and our ongoing studies show that SHG imaging will have great potential in gaining understanding of the construction and destruction of myofibrils within live cells and muscle tissue. Here we have observed that SHG in differentiating myocytes can appear either before or after α-actinin is localized in a periodic pattern. This implies that ordered thick filaments can arise independently of the establishment of structured Z-disks in the nascent myofibril, an observation that contradicts one prevailing model of sequential steps in myofibrillogenesis (52) and supports either the alternative model (53) or the possibility of more than one route to assembly of a mature myofibril. Within tissues, we find a variety of forms of myofibrillar disruption as part of normal and pathological muscle biology, and these features most likely represent localized degeneration and regeneration of the muscle fiber contractile apparatus (S. V. Plotnikov and W. A. Mohler, unpublished data).

Finally, in medical spectroscopy or imaging of tissue with ambiguous patterns of contrast, it may be desirable to identify the composition of SHG-bright material in situ (be it collagen, myosin, tubulin, or a mixture) without resorting to chemical or immunological analysis. Specific instances could

include scarring after damage to skeletal or cardiac muscle tissue or to the brain, as well as congenital fibrodysplasia ossificans progressiva (wherein cartilage and bone form ectopically within muscle) (54). Theoretical considerations and our data presented here suggest that the distinct SHG polarization anisotropy of different protein filaments might yield a spectrum of polarization dependence from such samples that could be unmixed to determine the identities and amounts of each component filament.

APPENDIX 1: THEORETICAL CONSIDERATIONS

Second-order susceptibility

The general description of nonlinear polarizability is given by the equation:

$$\mathbf{P} = \chi^{(1)} * \mathbf{E} + \chi^{(2)} * \mathbf{E} * \mathbf{E} + \chi^{(3)} * \mathbf{E} * \mathbf{E} * \mathbf{E} + \dots \tag{A1}$$

The polarization, $\mathbf{P}$, and the electric field, $\mathbf{E}$, are vectors and the nonlinear susceptibilities, $\chi^{(i)}$, are tensors. The general case of three-wave mixing, from two fields at frequencies ω_1 and ω_2 to a third field at $\omega_1 + \omega_2$, may be expressed at the bulk level as

$$P_i^{(2)}(\omega_1 + \omega_2) = \sum_{jk} \chi_{ijk}^{(2)}(\omega_1, \omega_2) E_j(\omega_1) E_k(\omega_2), \tag{A2}$$

or at the molecular level as

$$d_i^{(2)}(\omega_1 + \omega_2) = \sum_{jk} \beta_{ijk}(\omega_1, \omega_2) E_j(\omega_1) E_k(\omega_2). \tag{A3}$$

Here the dipole moment $d_i^{(2)}$ and hyperpolarizability β_{ijk} are the molecular analogues of the polarization (i.e., dipole moment per unit volume) $P_i^{(2)}$ and susceptibility $\chi_{ijk}^{(2)}$, respectively. Second harmonic generation is a degenerate case of three-wave mixing, such that $\omega_1 = \omega_2 = \omega$. Hence, from Eq. A2,

$$
\begin{aligned}
P_i^{(2)}(2\omega) &= \sum_{jk} \chi_{ijk}^{(2)}(\omega, \omega) E_j(\omega) E_k(\omega) \\
&= \sum_{kj} \chi_{ikj}^{(2)}(\omega, \omega) E_k(\omega) E_j(\omega) \\
&= \sum_{jk} \chi_{ikj}^{(2)}(\omega, \omega) E_j(\omega) E_k(\omega).
\end{aligned} \tag{A4}
$$

Therefore,

$$\chi_{ikj}^{(2)}(\omega, \omega) = \chi_{ijk}^{(2)}(\omega, \omega). \tag{A5}$$

Given this symmetry, a contracted notation (55) may be used,

$$d_{is}^{(2)}(\omega) = \chi_{ijk}^{(2)}(\omega, \omega), \tag{A6}$$

where i remains a spatial index with values running from 1 to 3 and s runs from 1 to 6 with the following relationships holding between s, j, and k.

$$
\begin{array}{ccc}
s & j & k \\
1 & 1 & 1 \\
2 & 2 & 2 \\
3 & 3 & 3 \\
4 & 2 & 3 \\
5 & 3 & 1 \\
6 & 1 & 2
\end{array} \tag{A7}
$$

A further simplification may be introduced if ω_1 and ω_2 are far from any natural frequencies—in other words off-resonance—in which case the susceptibility may be assumed independent of frequency,

$$\chi_{ijk}^{(2)}(\omega_1, \omega_2) \cong \chi_{ijk}^{(2)}. \tag{A8}$$

As a consequence, we may freely permute the indices as well, a condition known as Kleinman symmetry,

$$\chi_{ijk}^{(2)} = \chi_{ikj}^{(2)} = \chi_{jki}^{(2)} = \chi_{jik}^{(2)} = \chi_{kij}^{(2)} = \chi_{kji}^{(2)}. \tag{A9}$$

To summarize, the general case of three-wave mixing has $3 \times 3 \times 3 = 27$ independent elements in the susceptibility tensor, $\chi_{ijk}^{(2)}(\omega_1, \omega_2)$. Similarly, second harmonic generation has $3 \times 6 = 18$ independent elements in the contracted matrix, $d_{is}^{(2)}(\omega)$. Finally, when Kleinman symmetry holds there are only 10 independent elements.

Cylindrical symmetry

We now consider the properties of the susceptibility tensor under conditions of cylindrical symmetry, as is found in myosin and collagen filaments. For a general rotation from axes x', y', z' to x, y, z, the components of the susceptibility tensor transform as follows,

$$\chi_{ijk}^{(2)} = \sum_{i'j'k'} \cos\theta_{ii'} \cos\theta_{jj'} \cos\theta_{kk'} \chi_{i'j'k'}^{(2)}, \tag{A10}$$

where $\theta_{ii'}$ is the angle between the i' and i axes. (For simplicity we have not shown the frequency arguments of the susceptibility tensor.) For invariance under xy-rotations about the long axis of the cylinder, we find that

$$\chi_{zzz}^{(2)} = d_{33} = n \tag{A11}$$

$$\chi_{zxx}^{(2)} = \chi_{zyy}^{(2)} = d_{31} = m \tag{A12}$$

$$\chi_{xxz}^{(2)} = \chi_{xzx}^{(2)} = \chi_{yyz}^{(2)} = \chi_{yzy}^{(2)} = d_{15} = a \tag{A13}$$

$$\chi_{xyz}^{(2)} = \chi_{xzy}^{(2)} = -\chi_{yxz}^{(2)} = -\chi_{yzx}^{(2)} = d_{14} = b \tag{A14}$$

while all other components vanish. For cylindrical symmetry, therefore, there are only four independent elements, as represented by Mazely and Hetherington's single letter notations a, b, m, and n (56).

Single-axis molecules

We may also derive the bulk susceptibility from the molecular hyperpolarizability. For molecules oriented with some distribution of molecular axes x', y', z' relative to the bulk axes x, y, z,

$$\chi_{ijk}^{(2)} = \sum_{i'j'k'} < \cos\theta_{ii'} \cos\theta_{jj'} \cos\theta_{kk'} > \beta_{i'j'k'}, \tag{A15}$$

where the angle brackets signify averaging over molecules. For simplicity, we assume a molecule with a single preferred axis of hyperpolarizability,

$$\beta_{z'z'z'} = \beta, \tag{A16}$$

with all other components vanishing. Further assuming that the molecules are distributed with a constant polar angle, $\theta_{zz'} = \theta$, and a random azimuth angle, ϕ, we find that

$$\chi_{zzz}^{(2)} = n = N\cos^3\theta\,\beta \tag{A17}$$

$$\chi_{zxx}^{(2)} = m = N\cos\theta\sin^2\theta < \sin^2\phi > \beta = N/2\cos\theta\sin^2\theta\,\beta \tag{A18}$$

$$\chi_{xxz}^{(2)} = a = N/2\cos\theta\sin^2\theta\,\beta = m \tag{A19}$$

$$\chi_{xyz}^{(2)} = b = N\cos\theta\sin^2\theta < \cos\phi\sin\phi > \beta = 0. \tag{A20}$$

For a cylindrically symmetric distribution of single-axis molecules, therefore, there are only two independent elements and from their ratio may be calculated the characteristic polar angle, θ. (Note that the susceptibility tensor for this case also possesses Kleinman symmetry, even

though we have not assumed that β is off-resonance: the susceptibility tensor may still be dependent on frequency.) Such an arrangement may be obtained by having molecules randomly distributed in a monolayer (56) or by having them form ordered structures such as helices.

Analyzing polarization anisotropy data

From specific measurements, therefore, it is possible to calculate the characteristic angle. In general, we may set up an experiment such that, with the laser propagating along the y axis, the angle between the laser polarization and the sample (which lies in and defines the xz-plane) can be varied by turning the specimen on a rotating microscope stage. For measurements of this sort, we can write the polarization in a particularly clean form,

$$\mathbf{P}^{(2)} = a\,\mathbf{z}\,(\mathbf{z}\cdot\mathbf{E})^2 + b\,\mathbf{z}\,(\mathbf{E}\cdot\mathbf{E}) + c\,\mathbf{E}\,(\mathbf{z}\cdot\mathbf{E}), \qquad (A21)$$

where a, b, and c are numerical coefficients used by Stoller et al. (40,41,12) and $\mathbf{z}$ is the unit vector along the z axis (the long axis of the cylinder). Fitting the SHG signal as a function of laser polarization angle will thus give us values for a, b, and c. However, for either off-resonant Kleinman symmetry or single-axis molecules in a cylindrically symmetric arrangement, the three coefficients are not independent,

$$a = \chi^{(2)}_{zzz} - 3\chi^{(2)}_{zxx} = d_{33} - 3d_{31} = n - 3m \qquad (A22)$$

$$b = \chi^{(2)}_{zxx} = d_{31} = m \qquad (A23)$$

$$c = 2\chi^{(2)}_{zxx} = 2d_{31} = 2m. \qquad (A24)$$

Note that $c/b = 2$. If this is the case for the experimentally determined a, b, and c, then we may conclude either that the sample is off-resonance or that it is composed of single-axis molecules in a cylindrically symmetric arrangement and hence calculate the characteristic angle for a simple elemental dipole.

Myosin and collagen both form cylindrical arrays of polypeptide coils. However, the precise structure of the coils differs: whereas myosin coils are formed by α-helices, the coils of collagen comprise glycine-proline helices, with a much more extended rise-per-residue (2.9 Å, 3.3 residues/turn) than α-helices (1.5 Å, 3.6 residues/turn). From earlier data on muscle fibers by Sun and co-workers (12) we find that $c/b = 2.04$ and $\theta = 67.2°$, whereas our data yield $c/b = 1.94$ and $\theta = 61.2°$. In both cases the excitation, 1230 and 900 nm, respectively, is off-resonance for actomyosin, so that $c/b \approx 2$, and we find reasonable agreement between the calculated angles. By contrast, c/b for collagen, such as from rat-tail tendon (40,41) is significantly <2 for excitation wavelengths of 800, 850, 900, and 1064 nm, because excitation is not far off-resonance. Despite this fact, we find that θ calculated for collagen at each of these wavelengths (49.5° at 800 nm, 53.3° at 850 nm, 50.7° at 900 nm, 52.4° at 1064 nm) is comparable and coincides reasonably well with 45.3°, the known pitch angle for the collagen glycine-proline helix.

REFERENCES

1. Campagnola, P. J., and L. M. Loew. 2003. Second-harmonic imaging microscopy for visualizing biomolecular arrays in cells, tissues and organisms. *Nat. Biotechnol.* 21:1356–1360.

2. Millard, A. C., P. J. Campagnola, W. Mohler, A. Lewis, and L. M. Loew. 2003. Second harmonic imaging microscopy. *Methods Enzymol.* 361:47–69.

3. Kim, B.-M., J. Eichler, and L. B. Da Silva. 1999. Frequency doubling of ultrashort laser pulses in biological tissue. *Appl. Opt.* 38:7145–7150.

4. Stoller, P., B.-M. Kim, A. M. Rubinchik, K. M. Reiser, and L. B. Da Silva. 2001. Polarization-dependent optical second-harmonic imaging of a rat-tail tendon. *J. Biomed. Opt.* 7:205–214.

5. Campagnola, P. J., A. C. Millard, M. Terasaki, P. E. Hoppe, C. J. Malone, and W. A. Mohler. 2002. 3-dimensional high-resolution second harmonic generation imaging of endogenous structural proteins in biological tissues. *Biophys. J.* 82:493–508.

6. Yeh, A. T., N. Nassif, A. Zoumi, and B. J. Tromberg. 2002. Selective corneal imaging using combined second-harmonic generation and two-photon excited fluorescence. *Opt. Lett.* 27:2082–2084.

7. Brown, E., T. McKee, E. diTomaso, A. Pluen, B. Seed, Y. Boucher, and R. K. Jain. 2003. Dynamic imaging of collagen and its modulation in tumors in vivo using second-harmonic generation. *Nat. Med.* 9:796–800.

8. Cox, G., E. Kable, A. Jones, I. Fraser, F. Manconi, and M. D. Gorrell. 2003. 3-dimensional imaging of collagen using second harmonic generation. *J. Struct. Biol.* 141:53–62.

9. Dombeck, D. A., K. A. Kasischke, H. D. Vishwasrao, M. Ingelsson, B. T. Hyman, and W. W. Webb. 2003. Uniform polarity microtubule assemblies imaged in native brain tissue by second-harmonic generation microscopy. *Proc. Natl. Acad. Sci. USA.* 100:7081–7086.

10. Zipfel, W. R., R. M. Williams, R. Christie, A. Y. Nikitin, B. T. Hyman, and W. W. Webb. 2003. Live tissue intrinsic emission microscopy using multiphoton-excited native fluorescence and second harmonic generation. *Proc. Natl. Acad. Sci. USA.* 100:7075–7080.

11. Boulesteix, T., E. Beaurepaire, M. P. Sauviat, and M. C. Schanne-Klein. 2004. Second-harmonic microscopy of unstained living cardiac myocytes: measurements of sarcomere length with 20-nm accuracy. *Opt. Lett.* 29:2031–2033.

12. Chu, S.-W., S.-Y. Chen, G.-W. Chern, T.-H. Tsai, Y.-C. Chen, B.-L. Lin, and C.-K. Sun. 2004. Studies of (2)/(3) tensors in submicron-scaled bio-tissues by polarization harmonics optical microscopy. *Biophys. J.* 86:3914–3922.

13. Han, M., L. Zickler, G. Giese, M. Walter, F. H. Loesel, and J. F. Bille. 2004. Second-harmonic imaging of cornea after intrastromal femto-second laser ablation. *J. Biomed. Opt.* 9:760–766.

14. Sun, C.-K., S.-W. Chu, S.-Y. Chen, T.-H. Tsai, T.-M. Liu, C.-Y. Lin, and H.-J. Tsai. 2004. Higher harmonic generation microscopy for developmental biology. *J. Struct. Biol.* 147:19–30.

15. Zoumi, A., X. Lu, G. S. Kassab, and B. J. Tromberg. 2004. Imaging coronary artery microstructure using second-harmonic and two-photon fluorescence microscopy. *Biophys. J.* 87:2778–2786.

16. Williams, R. M., W. R. Zipfel, and W. W. Webb. 2005. Interpreting second-harmonic generation images of collagen i fibrils. *Biophys. J.* 88:1377–1386.

17. Zipfel, W. R., R. M. Williams, and W. W. Webb. 2003. Nonlinear magic: multiphoton microscopy in the biosciences. *Nat. Biotechnol.* 21:1369–1377.

18. Ouzounov, D. G., K. D. Moll, M. A. Foster, W. R. Zipfel, W. W. Webb, and A. L. Gaeta. 2002. Delivery of nanojoule femtosecond pulses through large-core microstructured fibers. *Opt. Lett.* 27:1513–1515.

19. Clark, K. A., A. S. McElhinny, M. C. Beckerle, and C. C. Gregorio. 2002. Striated muscle cytoarchitecture: an intricate web of form and function. *Annu. Rev. Cell Dev. Biol.* 18:637–706.

20. Noll, D., and H. Weber. 1934. Polariationsoptik und mlekularer feinbau der z-abschnitte des froschmuskels. *Pfluegers Archiv Gesamte Physiol. Menschen Tiere.* 235. [in German].

21. Colby, R. H. 1971. Intrinsic birefringence of glycerinated myofibrils. *J. Cell Biol.* 51:763–771.

22. Mohler, W., A. C. Millard, and P. J. Campagnola. 2003. Second harmonic generation imaging of endogenous structural proteins. *Methods.* 29:97–109.

23. Millard, A. C., L. Jin, M. D. Wei, J. P. Wuskell, A. Lewis, and L. M. Loew. 2004. Sensitivity of second harmonic generation from styryl dyes to transmembrane potential. *Biophys. J.* 86:1169–1176.

24. Szent-Gyorgyi, A. G., C. Cohen, and J. Kendrick-Jones. 1971. Paramyosin and the filaments of molluscan ''catch'' muscles. II. Native filaments: isolation and characterization. *J. Mol. Biol.* 56:239–258.

25. Knight, P. J., and J. A. Trinick. 1982. Preparation of myofibrils. *Methods Enzymol* 85 Pt B:9–12.

26. Dabiri, G. A., K. K. Turnacioglu, J. C. Ayoob, J. M. Sanger, and J. W. Sanger. 1999. Transfections of primary muscle cell cultures with plasmids coding for GFP linked to full-length and truncated muscle proteins. *Methods Cell Biol.* 58:239–260.

27. Kurokawa, H., W. Fujii, K. Ohmi, T. Sakurai, and Y. Nonomura. 1990. Simple and rapid purification of brevin. *Biochem. Biophys. Res. Commun.* 168:451–457.

28. Hidalgo, C., R. Padron, R. Horowitz, F. Q. Zhao, and R. Craig. 2001. Purification of native myosin filaments from muscle. *Biophys. J.* 81:2817–2826.

29. Laemmli, U. K. 1970. Cleavage of structural proteins during the assembly of the head of bacteriophage t4. *Nature.* 227:680–685.

30. Sanger, J. W., B. Mittal, and J. M. Sanger. 1984. Analysis of myofibrillar structure and assembly using fluorescently labeled contractile proteins. *J. Cell Biol.* 98:825–833.

31. Zhukarev, V., J. M. Sanger, J. W. Sanger, Y. E. Goldman, and H. Shuman. 1997. Distribution and orientation of rhodamine-phalloidin bound to thin filaments in skeletal and cardiac myofibrils. *Cell Motil. Cytoskeleton.* 37:363–377.

32. Bukatina, A. E., B. Y. Sonkin, L. L. Alievskaya, and V. A. Yashin. 1984. Sarcomere structures in the rabbit psoas muscle as revealed by fluorescent analogs of phalloidin. *Histochemistry.* 81:301–304.

33. Gordon, A. M., A. F. Huxley, and F. J. Julian. 1966. The variation in isometric tension with sarcomere length in vertebrate muscle fibres. *J. Physiol.* 184:170–192.

34. Hanson, J., and H. E. Huxley. 1957. Quantitative studies on the structure of cross-striated myofibrils. II. Investigations by biochemical techniques. *Biochim. Biophys. Acta.* 23:250–260.

35. Gregorio, C. C., and V. M. Fowler. 1995. Mechanisms of thin filament assembly in embryonic chick cardiac myocytes: tropomodulin requires tropomyosin for assembly. *J. Cell Biol.* 129:683–695.

36. Margulis, B. A., and G. P. Pinaev. 1976. The species specifity of the contractile protein composition of the bivalve molluscs. *Comp. Biochem. Physiol. B.* 55:189–194.

37. Waterston, R. H. 1988. The Nematode *Caenorhabaditis elegans.* W. B. Wood, editor. Cold Spring Harbor Laboratory, Cold Spring Harbor, New York.

38. Barnett, V. A. 2001. Cross-bridge cooperativity during isometric contraction and unloaded shortening of skeletal muscle. *J. Muscle Res. Cell Motil.* 22:415–423.

39. Schoenberg, M. 1989. Effect of adenosine triphosphate analogues on skeletal muscle fibers in rigor. *Biophys. J.* 56:33–41.

40. Stoller, P., B. M. Kim, A. M. Rubenchik, K. M. Reiser, and L. B. Da Silva. 2002. Polarization-dependent optical second-harmonic imaging of a rat-tail tendon. *J. Biomed. Opt.* 7:205–214.

41. Stoller, P., K. M. Reiser, P. M. Celliers, and A. M. Rubenchik. 2002. Polarization-modulated second harmonic generation in collagen. *Biophys. J.* 82:3330–3342.

42. Beck, K., and B. Brodsky. 1998. Supercoiled protein motifs: the collagen triple-helix and the alpha-helical coiled coil. *J. Struct. Biol.* 122:17–29.

43. Conboy, J. C., and M. A. Kriech. 2003. Measuring melittin binding to planar supported lipid bilayer by chiral second harmonic generation. *Anal. Chim. Acta.* 496:143–153.

44. Kriech, M. A., and J. C. Conboy. 2003. Label-free chiral detection of melittin binding to a membrane. *J. Am. Chem. Soc.* 125:1148–1149.

45. Mitchell, S. A., R. A. McAloney, D. Moffatt, N. Mora-Diez, and M. Z. Zgierski. 2005. Second-harmonic generation optical activity of a polypeptide alpha-helix at the air/water interface. *J. Chem. Phys.* 122:114707.

46. Millman, B. M., and P. M. Bennett. 1976. Structure of the cross-striated adductor muscle of the scallop. *J. Mol. Biol.* 103:439–467.

47. Wray, J. S. 1979. Structure of the backbone in myosin filaments of muscle. *Nature.* 277:37–40.

48. Epstein, H. F., D. M. Miller III, I. Ortiz, and G. C. Berliner. 1985. Myosin and paramyosin are organized about a newly identified core structure. *J. Cell Biol.* 100:904–915.

49. Epstein, H. F., G. Y. Lu, P. R. Deitiker, I. Oritz, and M. F. Schmid. 1995. Preliminary three-dimensional model for nematode thick filament core. *J. Struct. Biol.* 115:163–174.

50. Skubiszak, L., and L. Kowalczyk. 2002. Myosin molecule packing within the vertebrate skeletal muscle thick filaments. A complete bipolar model. *Acta Biochim. Pol.* 49:829–840.

51. Skubiszak, L., and L. Kowalczyk. 2002. The vertebrate skeletal muscle thick filaments are not three-stranded. Reinterpretation of some experimental data. *Acta Biochim. Pol.* 49:841–853.

52. Sanger, J. W., P. Chowrashi, N. C. Shaner, S. Spalthoff, J. Wang, N. L. Freeman, and J. M. Sanger. 2002. Myofibrillogenesis in skeletal muscle cells. *Clin Orthop Relat Res*:S153–62.

53. Gregorio, C. C., and P. B. Antin. 2000. To the heart of myofibril assembly. *Trends Cell Biol.* 10:355–362.

54. Shore, E. M., F. H. Gannon, and F. S. Kaplan. 1997. Fibrodysplasia ossificans progressiva: why do some people have two skeletons? *Rev. Rhum. Engl. Ed.* 64:92S–97S.

55. Boyd, R. W. 1992. Nonlinear Optics. Academic Press, San Diego, CA.

56. Mazely, T. L., and W. M. Hetherington III. 1987. Second-order susceptibility tensors of partially ordered molecules on surfaces. *J. Chem. Phys.* 86:3640–3647.

57. Tameyasu, T. 1994. Oscillatory contraction of single sarcomere in single myofibril of glycerinated, striated adductor muscle of scallop. *Jpn. J. Physiol.* 44:295–318.